

Qing, J., Liao, J., Brune, S. (2024): Rift Propagation Interacting With Pre-Existing Microcontinental Blocks. - Journal of Geophysical Research: Solid Earth, 129, 3, e2023JB028109.




<https://doi.org/10.1029/2023JB028109>

# JGR Solid Earth

## RESEARCH ARTICLE

10.1029/2023JB028109

## Rift Propagation Interacting With Pre-Existing Microcontinental Blocks

Jiarong Qing<sup>1</sup> , Jie Liao<sup>1,2,3</sup> , and Sascha Brune<sup>4,5</sup> 

<sup>1</sup>School of Earth Sciences and Engineering, Sun Yat-sen University, Guangzhou, China, <sup>2</sup>Southern Marine Science and Engineering Guangdong Laboratory (Zhuhai), Zhuhai, China, <sup>3</sup>Guangdong Provincial Key Lab of Geodynamics and Geohazards, Guangzhou, China, <sup>4</sup>GFZ German Research Centre for Geosciences, Potsdam, Germany, <sup>5</sup>Institute of Geosciences, University of Potsdam, Potsdam, Germany

### Key Points:

- Pre-existing microcontinental blocks affect rift propagation
- Lithospheric heterogeneities play a dominant role in rift propagation patterns
- Model results elucidate rift propagation patterns in the South China Sea, the East African Rift System, and the Woodlark Basin

### Supporting Information:

Supporting Information may be found in the online version of this article.

### Correspondence to:

J. Liao,  
liaojie5@mail.sysu.edu.cn

### Citation:

Qing, J., Liao, J., & Brune, S. (2024). Rift propagation interacting with pre-existing microcontinental blocks. *Journal of Geophysical Research: Solid Earth*, 129, e2023JB028109. <https://doi.org/10.1029/2023JB028109>

Received 19 OCT 2023

Accepted 5 FEB 2024

### Author Contributions:

**Conceptualization:** Jiarong Qing, Jie Liao, Sascha Brune

**Investigation:** Jiarong Qing

**Methodology:** Jiarong Qing

**Supervision:** Jie Liao

**Visualization:** Jiarong Qing

**Writing – original draft:** Jiarong Qing, Jie Liao

**Writing – review & editing:**

Jiarong Qing, Jie Liao, Sascha Brune

**Abstract** Rift propagation is a 3D thermo-mechanical process that often precedes continental breakup. Pre-existing microcontinental blocks and the associated lithospheric strength heterogeneities influence the style of rift propagation. Interestingly, some rifts propagate into pre-existing blocks and eventually cut through them (e.g., the Zhongsha Block and the Reed Bank), while others bypass these microcontinental blocks forming distinct overlapping rift branches (e.g., the East African Rift System). In this study, we use 3D numerical models to investigate the interaction between microcontinental blocks and rift propagation under different far-field extension rates. In doing so, we assess the impact of mantle lithospheric thicknesses and lower crustal rheology on the style of rift propagation. Our models reproduce the two types of rift propagation, characterized by propagating rifts that either split or bypass the pre-existing microcontinental blocks. We find that lithospheric thickness exerts dominant control, while lower crustal rheology of microcontinental blocks and the extension rate have less effect on rift propagation. Our model results can explain rift propagation patterns, block rotation and strong lithospheric thinning in the South China Sea, the East African Rift System, and the Woodlark Basin.

**Plain Language Summary** Rift propagation is an essential process during continental rifting, which rarely follows a straight line due to the heterogeneous nature of continental lithosphere. Here, we use 3D geodynamic numerical modeling to simulate the dynamic evolution of rift propagation interacting with pre-existing microcontinental blocks. We find that rift propagation is inhibited by strong microcontinental blocks with thick mantle lithosphere, while it splits through weaker microcontinental blocks. We suggest that the strength of microcontinental blocks explains the observed pattern of rift propagation in the South China Sea, the East African Rift System, and the Woodlark Basin.

## 1. Introduction

Rift propagation is a wide-spread process during continental rifting and break up. It is an intrinsically three-dimensional process that is characterized by along-strike changes in rift maturity, crustal thickness, and lithospheric strength. Two alternative kinematic mechanisms of rift propagation have been identified in previous studies. One is rotational opening, which takes place when rifting occurs near the Euler pole and leads to along-strike changes in total extension (Bellahsen et al., 2003; Molnar et al., 2017; Mondy et al., 2018; Zwaan et al., 2020). The second mechanism is rift propagation due to along-strike variations in rift lithology (Balázs et al., 2023; Gouiza & Naliboff, 2021; Koehn et al., 2008; Van Wijk & Blackman, 2005; Vink, 1982).

Microcontinental blocks are common features in extensional tectonic areas. Major examples are the Sao Paulo Plateau (Neuharth et al., 2021), the Flemish Cap offshore eastern Canada (Srivastava et al., 2000), the Tanzania Craton in the East African Rift System (Nyblade & Brazier, 2002). The strength contrast of such blocks relative to neighboring lithosphere likely affects rift propagation (Courtillot, 1982; Dunbar & Sawyer, 1996; Manighetti et al., 1997, 1998). Many microcontinental blocks feature petrological characteristics that are different from the surrounding lithosphere, either because of a different lithospheric age or due to spatially variable deformation histories. The strength of the continental lithosphere can be increased as a function of various factors, including mafic lower crustal rheology, thicker mantle lithosphere, and Precambrian continental basement (Audet & Bürgmann, 2011; Heron & Pysklywec, 2016; Pasyanos et al., 2014; X. Sun et al., 2014). Further studies indicate that the formation of microcontinental blocks depends on the strength of the lithosphere under various conditions of tectonic forces (Whittaker et al., 2016), rift interaction (King & Welford, 2022a, 2022b), insufficient magmatism (Abera et al., 2016; Huang et al., 2020), and intense metamorphism (X. Sun et al., 2014).

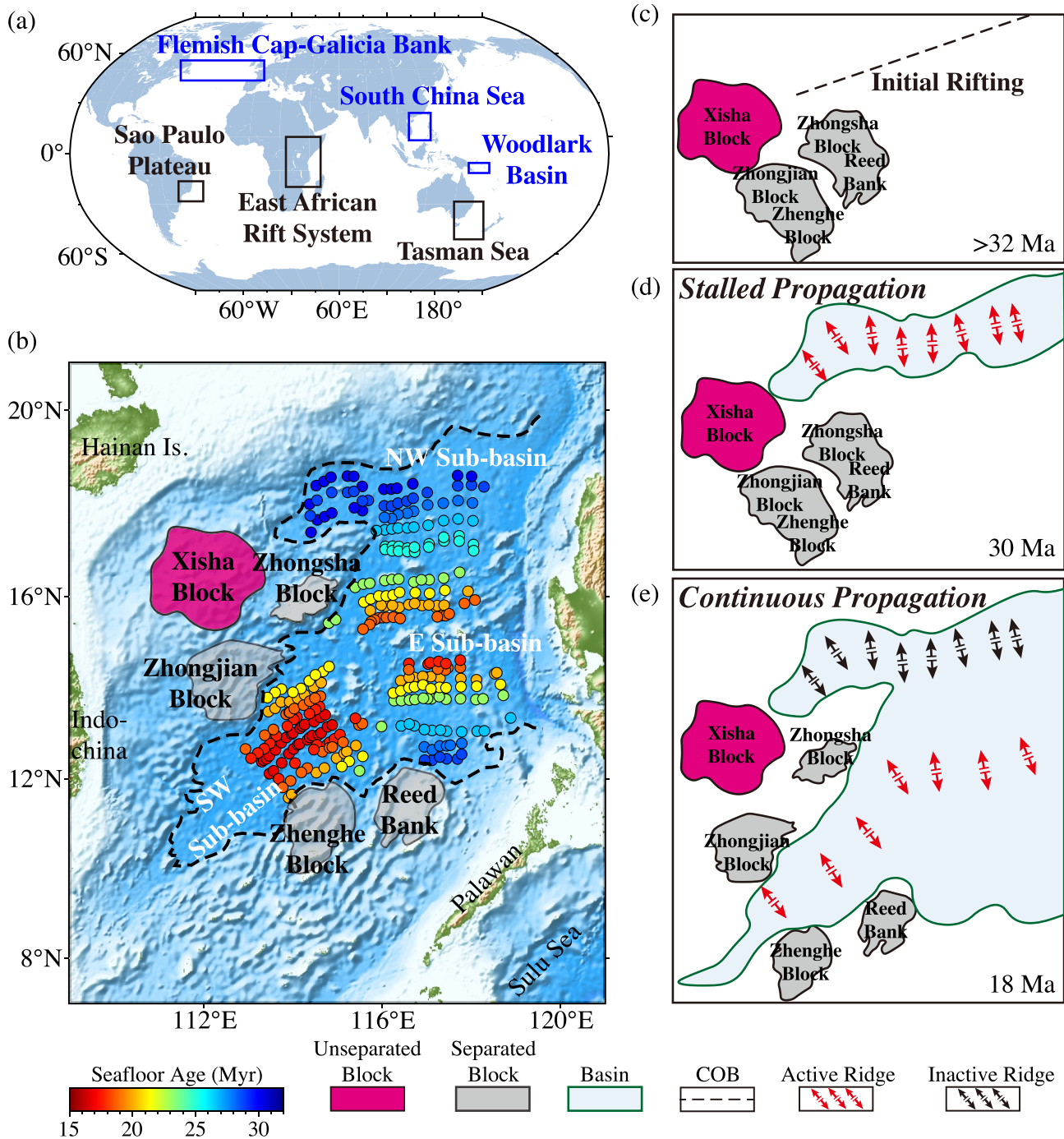


**Figure 1.** Examples of rift propagation interacting with pre-existing microcontinental blocks. (a) Location of natural examples. Blue and black color indicates whether rift propagation split or bypassed the microcontinental blocks, respectively. (b) Simplified tectonic setting of the South China Sea. The extent of the microcontinental blocks is indicated by irregular circles (modified from Ding & Li, 2016). Gray shading indicates microcontinental blocks that were once separated by rift propagation. Magenta shading indicates microcontinental blocks that stalled rift propagation. The colored circles represent oceanic crustal age (Briais et al., 1993; Seton et al., 2014). (c–e) Plate kinematic sketches of the South China Sea (SCS) formation at different epochs (modified from Briais et al., 1993; Ding & Li, 2016; Sibuet et al., 2016). We hypothesize that the interaction between microcontinental blocks and rift propagation controls the first-order structure of a rift.

Some natural examples show that rifts propagate forward by splitting microcontinental blocks located in front of the rift tip (e.g., the Southwest South China Sea, the Woodlark Basin, the Flemish Cap-Galicia Bank, Figures 1a and 1b). Other examples show that rift propagation can be inhibited by microcontinental blocks leading to the formation of distinct rift branches and to rotating blocks (e.g., the Northwest South China Sea, Tasman Sea, Sao

Paulo Plateau, the East African Rift System, Figures 1a and 1b). As the largest marginal ocean basin in the western Pacific, the South China Sea (SCS) is a typical example where rift propagation has been affected by pre-existing microcontinental blocks (i.e., the Xisha Block, Zhongsha Block, Reed Bank, Zhongjian Block, Zhenghe Block, Figure 1b). Previous studies indicate that the Zhongsha Block and the Zhongjian Block were connected to the Reed Bank and the Zhenghe Block during rifting and break-up processes, respectively (Pichot et al., 2014; Wei et al., 2015). Under the influence of microcontinental blocks, rift propagation shows two types of features. At 30 Ma, the active rift was blocked by the Xisha block such that the spreading ridge could not propagate forward (Figures 1c and 1d). At this time, the microcontinental block did not deform dramatically and the deformation was concentrated in narrow troughs (i.e., Xisha trough, Li et al., 2021). Subsequently, the active rift migrated southward and formed a new ridge segment that was driven by the southward subduction of the proto-South China Sea (Figures 1e, Zahirovic et al., 2014). Finally, the continental rift smoothly propagated through the Zhongsha Block-Reed Bank and the Zhongjian-Zhenghe blocks (Figure 1e).

Previous studies suggest that far-field and local stresses, surface processes, mantle flow and magmatism can influence rift propagation, leading to different directions and shapes (Jourdon et al., 2020; Schmid et al., 2023; Steinberger et al., 2019; Sternai et al., 2021; Z. Sun et al., 2009). However, it is unclear how the rift propagation interacts with pre-existing microcontinental blocks. In this study, we investigate the dynamics of rift propagation in the presence of pre-existing lithospheric heterogeneities by using 3D thermo-mechanical numerical models. We vary three parameters of pre-existing blocks in this model: mantle lithospheric thickness, extension rate and lower crustal rheology and identify their impact on first-order rift propagation patterns. Finally, we compare representative models with three natural rifts, the South China Sea, the East African Rift System and the Woodlark Basin.

## 2. Method

### 2.1. Numerical Methods

The 3D thermo-mechanical numerical code I3ELVIS (Gerya, 2013; Gerya & Yuen, 2003), which is based on finite-differences and marker-in-cell techniques is used to simulate rift propagation affected by pre-existing microcontinental blocks. The conservation equations of mass, momentum, and energy are solved in a fully staggered grid assuming an incompressible medium:

$$\frac{\partial v_i}{\partial x_i} = 0 \quad (1)$$

$$\frac{\partial \sigma'_{ij}}{\partial x_j} - \frac{\partial P}{\partial x_i} = -\rho g_i \quad (2)$$

$$\rho C_p \frac{DT}{Dt} = \frac{\partial}{\partial x_i} \left( k \frac{\partial T}{\partial x_i} \right) + H_r + H_s + H_a + H_L \quad (3)$$

where  $v$  is velocity,  $\sigma'$  the deviatoric stress tensor,  $P$  the total pressure (mean normal stress),  $\rho$  density,  $g$  gravitational acceleration,  $C_p$  heat capacity,  $T$  temperature,  $k$  thermal conductivity,  $H$  internal heating,  $H_s$  shear heating ( $H_s = \sigma'_{ij} \dot{\epsilon}_{ij}$ ,  $\dot{\epsilon}$  strain rate tensor),  $H_a$  adiabatic heating ( $H_a = T \alpha \frac{DP}{Dt}$ ,  $\alpha$  thermal expansivity),  $H_r$  radioactive heating with a constant value for each rock, and  $H_L$  latent heating included implicitly by increasing the effective heat capacity and thermal expansion of the partially crystallized/molten rocks (Burg & Gerya, 2005). The Einstein notation is used for the indexes  $i$  and  $j$ , which denote spatial directions  $i = (x,y,z)$  and  $j = (x,y,z)$  in 3D. The multigrid method is used to speed up the convergence of the Gauss–Seidel iterations for the coupled solve of Equations 1 and 2.

We employ visco-plastic rheology in our models. The non-Newtonian viscous rheology is strain rate-, pressure-, and temperature-dependent. Plastic rheology is described by a Drucker–Prager yield criterion, where the yield stress ( $\sigma_y$ ) is pressure dependent ( $C$  is rock cohesion and  $\mu$  is the effective friction coefficient). Viscosity due to plastic deformation ( $\eta_{plas}$ ) is computed based on the square root of the second invariant of strain rate ( $\dot{\epsilon}_{II}$ ). Eventually, the effective viscosity of rocks ( $\eta_{eff}$ ) is constrained by both viscous and plastic deformation. See further explanation of variables/symbols in Table S1 in Supporting Information S1.

$$\eta_{vis} = \frac{1}{2} A^{\frac{1}{2}} \dot{\epsilon}_{\Pi}^{\frac{1-n}{n}} \exp\left(\frac{PV_a + E_a}{nRT}\right)$$

$$\sigma_y = C + P\phi$$

$$\eta_{plas} = \frac{\sigma_y}{2\dot{\epsilon}_{\Pi}}$$

$$\eta_{eff} = \min(\eta_{vis}, \eta_{plas})$$

The lithospheric surface is calculated dynamically as an essentially internal free surface by using a layer of “sticky air” (Crameri et al., 2012). The layer is composed of “air” (1 kg/m<sup>3</sup>, 20 km in Y direction) which has a low viscosity (10<sup>19</sup> Pa s). Lower viscosity and/or greater air thickness can minimize the shear stress (<10<sup>5</sup> Pa) below the free surface (Burg & Gerya, 2005) and behave similarly to a true free surface, which is constrained by the numerical multigrid solver. Thus, for simplicity, surface erosion and sedimentation are neglected to some extent.

Sedimentation and erosion processes are implemented in a simplified way. During model development and the related crustal surface deformation, transformation of sticky air markers into sticky water occurs when these markers move below the prescribed water level (i.e., 3 km below the initial crustal surface). Further transformation of water markers into sediments occurs below the prescribed sedimentation level (i.e., 5 km below the initial crustal surface). Instantaneous erosion is prescribed at 5 km above the initial crustal level by converting rock markers to sticky air.

See further explanation of variables/symbols in Table S1 in Supporting Information S1 (Clauser & Huenges, 1995; Ranalli, 1995).

## 2.2. Model Setup

The numerical model contains 325 (X-axis) by 101 (Y-axis) by 373 (Z-axis) regular distributed nodes which corresponds to a physical dimension of 1,296 km by 400 km by 1,488 km (Figure 2). Vertically, the model box is composed of multiple lithological layers (i.e., continental upper/lower crust, lithosphere mantle and asthenosphere mantle). A microcontinental block is imposed near the center of the model (i.e.,  $x = 300\text{--}600$  km,  $y = 20\text{--}140$  km,  $z = 594\text{--}894$  km). The viscous flow laws of “mafic granulite” and “felsic granulite” describe the behavior of the lower crust of the microcontinental block and normal crust, respectively. Wet quartz rheology was used in the upper crust of the whole model. To facilitate rift initiation on one side, we set a weak zone in upper crust and lithosphere mantle, which is far away from the microcontinental block (i.e.,  $x = 1,000\text{--}1,296$  km).

A constant temperature boundary condition is employed at the upper and lower boundaries, and zero horizontal heat flux across the vertical boundaries. The initial temperature field is prescribed using a linear temperature profile between surface (with 0°C) and lithosphere-asthenosphere boundary (LAB) (at 1300°C). Below the LAB, the temperature gradient is 0.5°C/km. The LAB temperature of microcontinental blocks is equal to the thickness above normal lithosphere multiplied by 0.5°C/km. An additional boundary condition is prescribed to achieve extension with an irregular velocity, that is, 0.5 cm/yr in the lithosphere and decrease to zero in the asthenosphere (Figure 2b). Corresponding compensation velocities are employed at the bottom boundaries, allowing for the conservation of rock volume (Figure 2b).

We conduct a series of models where we assess the impact of the following factors on rift propagation: (a) homogenous lithosphere without pre-existing block (Figure 2c, Figure S1 in Supporting Information S1), (b) extension rate, (c) lower crustal rheology of the block and (d) lithospheric thickness of the block (Figures 2d and 2e).

## 3. Model Results

We conduct a series of numerical models to investigate how rift propagation interacts with a pre-existing microcontinental block. The model results suggest two types of deformation. Type-I models feature continuous rift propagation with microcontinental block splitting, and Type-II models are characterized by discontinuous rift

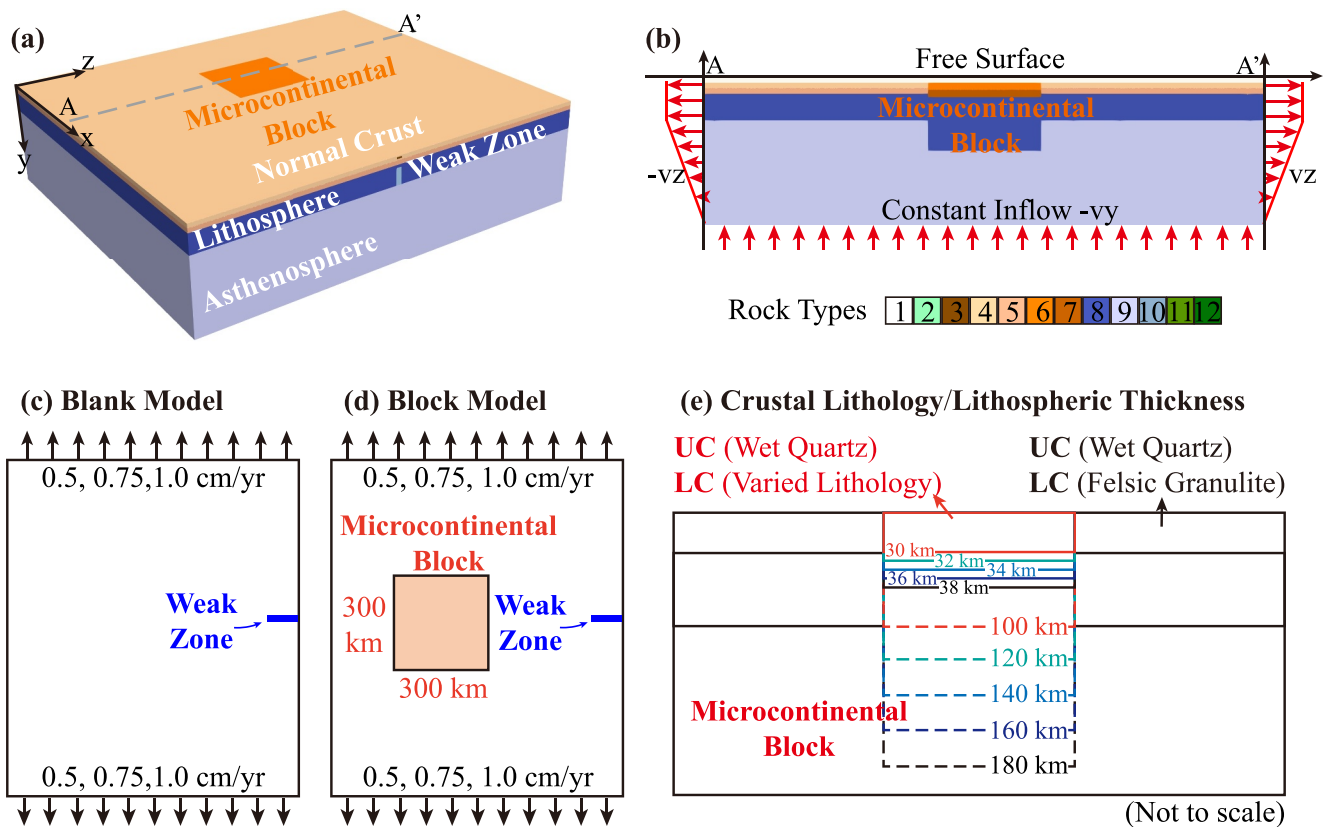


**Figure 2.** Numerical model setup. (a) Initial 3D geometry. (b) Vertical cross-section shows the configuration of the microcontinental block and velocity boundary conditions. Colors indicate rock types (also for all following figures) specified by the color codes: 1, air; 2, water; 3, sediment; 4, reference upper crust; 5, reference lower crust; 6, upper crust of microcontinental block; 7, lower crust of microcontinental block; 8, lithosphere; 9, asthenosphere; 10, weak zone; 11–12, oceanic crust. (c) Blank model setup without microcontinental block. Microcontinental block models with variations of (d) extension rate, (e) rheology of lower crust (i.e., felsic granulite, plagioclase, diabase, and mafic granulite) and lithospheric thickness (i.e., 100, 120, 140, 160, 180 km).

propagation with deformation occurring in specific parts of the microcontinental block and in adjacent ridge segments.

### 3.1. Continuous Rift Propagation Splitting the Microcontinental Block (Type-I Models)

In the early stage of Type-I models, the spreading center forms on one side of the model in response to the prescribed weak zone (Figure 3a, cross section CC'). Subsequently, the spreading center propagates to the other side of the model and splits the pre-existing microcontinental block (Figure 3b, cross section BB'), which is slightly stronger (due to its lower crust, prescribed by the rheology of mafic granulite) than the surrounding lithosphere. Type-I models result in a symmetric split of continental lithosphere and block (Figure 3c).

### 3.2. Discontinuous Rift Propagation Affected by the Microcontinental Blocks (Type-II Models)

The dynamic evolution of the Type-II models is characterized by discontinuous rift propagation (Figures 4 and 5). In terms of the deformation intensity of the blocks, we categorize the models into Type-IIA (Figure 4) and Type-IIB (Figure 5). The Type-IIA model is a transitional model, characterized by offset rift propagation (i.e., the formation of rift branches adjacent to the block) and a certain amount of microcontinental block splitting (Figure 4). In contrast to the continuous rift propagation model, this type of model features blocks with thicker mantle lithosphere that significantly hinder rift propagation. Two rift segments form on either side of the blocks due to their increasing strength (Figures 4a and 4b, cross section BB'). Although the propagating rift deforms the microcontinental block, it fails to fully break it, and deformation instead gets deflected right-laterally forming a

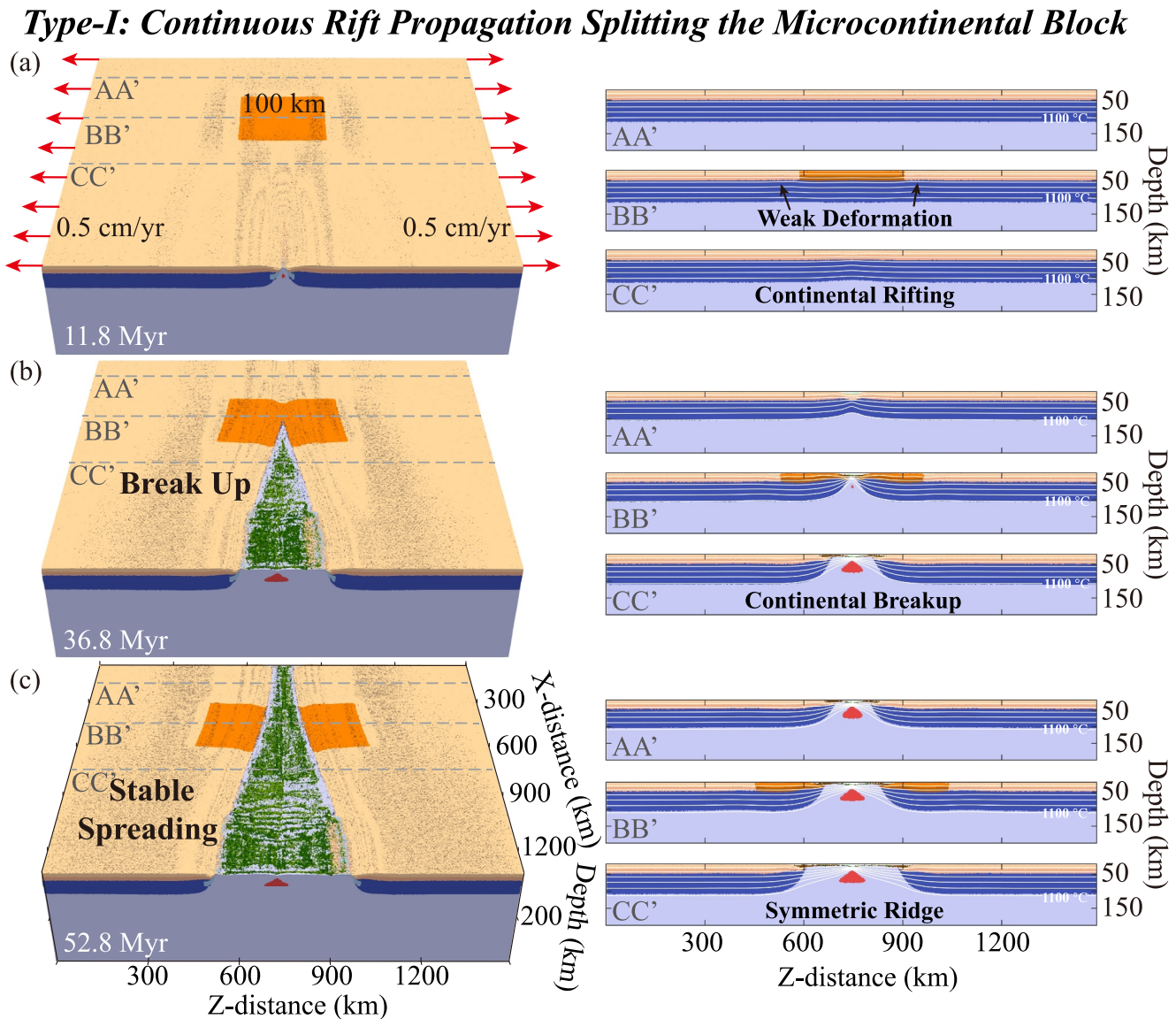


**Figure 3.** Evolution of the Type-I continuous rift propagation model. (a–c) Model results at 11.8, 36.8, and 52.8 Myr, respectively. Left panels: 3D visualization. Gray dashed lines show the locations of the cross sections displayed in the right panels. White lines in right panels represent the isotherms interval 200°C in lithosphere. This model shows that relatively weak microcontinental blocks cannot inhibit rift propagation and are split apart in a symmetric manner.

new rift segment (Figure 4c, cross section BB'). The formation of the new rift branch terminates the rift propagation and leads to an intense counterclockwise rotation of the central block (Figure 4d, cross section BB').

By further increasing the strength of the microcontinental block (e.g., via increasing its mantle lithospheric thickness, Figure 2f), we obtain the Type-IIB model. This type of model is characterized by negligible deformation of the block while the rift fully bypasses the strong lithospheric heterogeneity (Figure 5). The microcontinental block largely inhibits the rift propagation and promotes the formation of two rift branches outboard of the block (Figures 5b and 5c). These two rift arms compete such that if one rift branch is weaker than the other and ultimately succeeds in continental rupture, this branch will transition to sea floor spreading while the other will be abandoned (Figures 4d and 5d, cross section BB'). The mechanism of rift competition between these two branches involves non-linear weakening and strength feedback, resulting in the symmetry between the two branches being randomly broken (Brune et al., 2023). In the end, the microcontinental block remains unruptured and becomes a part of the plate to the left of the spreading ridge (Figure 5d). Where two ridge segments converge, they tend to form asymmetric ocean basins (Figure 5, cross section CC').

**Type-IIA: Discontinuous Rift Propagation with Intensive Block Deformation**

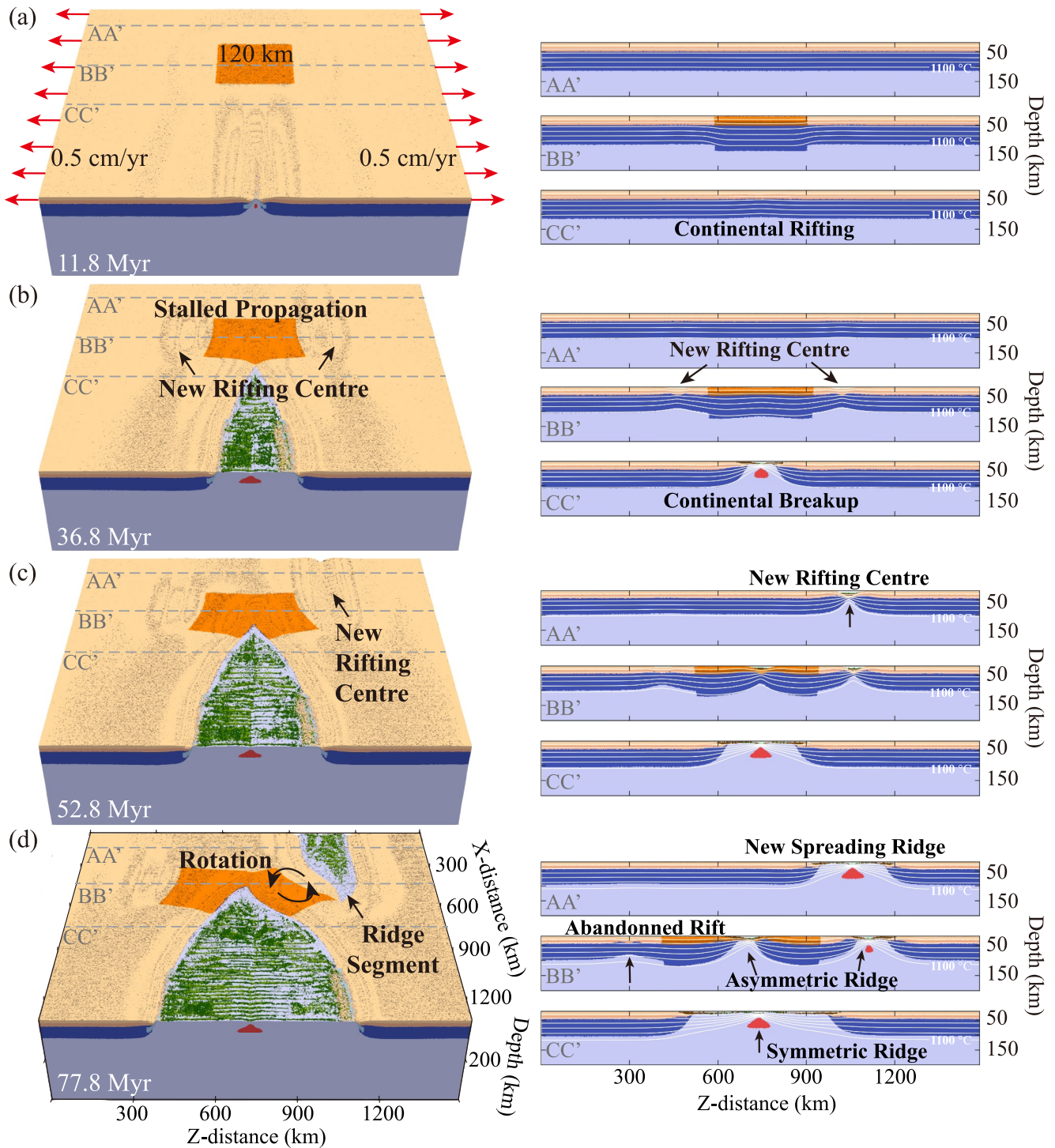


**Figure 4.** Evolution of the discontinuous rift propagation seen in Type-IIA model (the lithospheric thickness of the microcontinental block is 120 km and all other parameters are identical to the Type-I model). (a–d) Model results at 11.8, 36.8, 52.8, and 77.8 Myr, respectively. Left panels: 3D visualization. Gray dashed lines show the locations of the cross sections displayed in the right panels. White lines in right panels represent lithospheric isotherms in 200°C intervals. This model shows that relatively strong microcontinental blocks inhibit rift propagation but can still be deformed and partially split.



**Type-II B: Discontinuous Rift Propagation with Negligible Block Deformation**

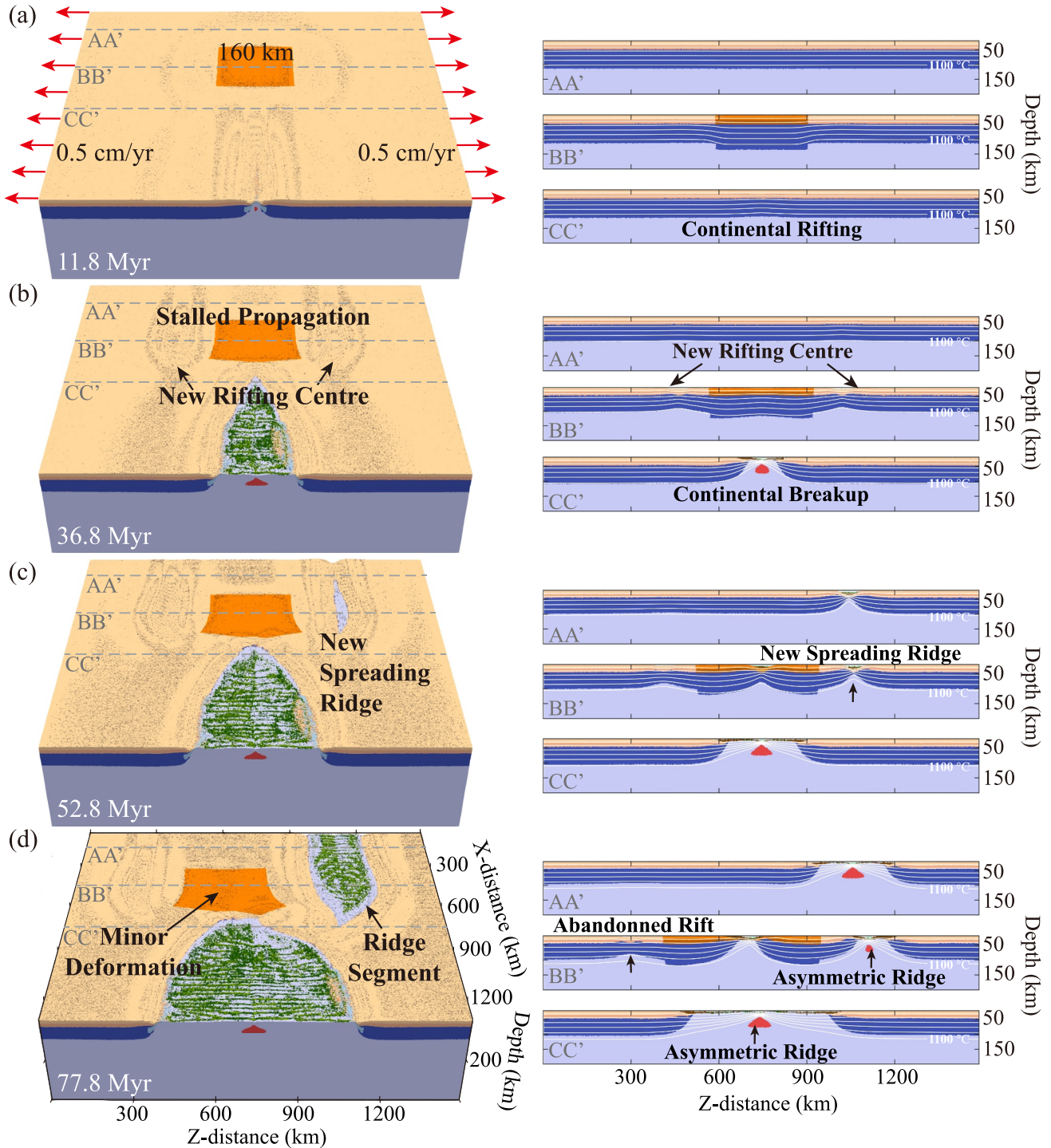


**Figure 5.** Evolution of the discontinuous rift propagation seen in Type-II B model (the lithospheric thickness of the microcontinental block is 160 km and the rest parameters are identical the Type-I model). (a–d) Model results at 11.8, 36.8, 52.8 and 77.8 Myr, respectively. Left panels: 3D visualization. Gray dashed lines show the locations of the cross sections displayed in the right panels. White lines in right panels represent lithospheric isotherms in 200°C intervals. This model shows that strong microcontinental blocks fully inhibit rift propagation. The block experiences only minor deformation and remains intact.

### 3.3. Parameter Variations

We conduct a series of numerical models to investigate the influence of different model parameters (i.e., lithospheric thickness of the microcontinental block, extension rate, and lower crustal rheology). The imposed microcontinental block in our models represents various continental terranes observed in nature (e.g., Prodehl & Mooney, 2012), ranging from relatively young Cenozoic orogenic belts (with thin lithosphere) to old Archean cratons (with thick lithosphere). For simplicity, we use lithospheric thickness as a proxy for the rigidity of various continental terranes. We assess the impact of microcontinental block strength by varying its lithospheric thickness from 100 to 180 km (Figure 2e). Model results suggest that with increased lithospheric thickness, the pattern of rift propagation changes from continuous propagation to discontinuous propagation (Figure 6a). Rift propagation is strongly inhibited, forming overlapping ridge segments and the deformation of the microcontinental block becomes negligible.

We assess the influence of lower crustal rheology and extension rate on rift propagation using the reference model with 100 km of lithospheric thickness (Figures 2d and 2e). Note that mechanical strength increases gradually from more felsic rheology to more mafic rheology. The model results suggest that crustal rheology and extension rate play a minor role in rift propagation (Figure 6b, Figure S1 in Supporting Information S1). In the low extension rate model (i.e., 0.5 cm/yr), the increase in mechanical strength of the lower crust did not cause a change in the propagation pattern (Figure 6b). However, in the high extension rate model (i.e., 0.75, 1.0 cm/yr), the influence of lower crust rheology is enhanced (Figure 6b).

Further quantitative analysis shows that the propagation distance of the first ridge segment decreases significantly as the lithosphere thickens (Figure 7a). The evolution of tectonic forces shows a characteristic pattern: the force required to maintain the prescribed boundary velocities initially increase and then immediately decrease in response to continental strength loss in the weak zone (Figures 3a, 4a, 5a, and 7b). As the rift propagates toward the microcontinental blocks, discontinuous rift propagation models show larger tectonic forces than continuous rift propagation models due to the thick mantle lithosphere. Lower crustal rheology has less effect on tectonic forces in continuous rift propagation. Higher extension rates necessitate significantly higher tectonic forces, favor rapid strain localization and promote rapid rift propagation (Figure 7c). Another interesting phenomenon relates to vertical-axis block rotation. The angle of rotation significantly decreases with increasing lithospheric thickness, while the extension rate and lower crustal rheology exert less effect on block rotation (Figure 6, Figure S2 in Supporting Information S1).

### 3.4. Comparison of Model Results

The models presented in this study show that interaction between propagating rifts and microcontinental blocks may give rise to a broad range of deformation patterns. In addition, these models exhibit a major time-dependence of stress patterns. We compute the Regime Stress Ratio value to illustrate the evolution of predominant stress regime and thereby the fault type in Figure 8 (see methods in the Text S2, e.g. Brune, 2014). In the early stage of the Type-I continuous rift propagation model, normal faults largely dominate all model types (Figure 8). Compressional stress regimes develop on both sides of the rift, associated with GPE gradients and bending of the lithosphere during rift shoulder formation. As the strength of the microcontinental block increases, rift propagation is strongly inhibited by the block. The notable difference of the Type-II discontinuous rift propagation model is the different distribution of normal faults, which is determined by the strength of microcontinental block (Figures 8e-l). As the microcontinental block becomes stronger, the propagation of the first rift stops in front of or within the microcontinental block (Figures 8g and 8k). The normal faults tend to be more concentrated at the edges of the microcontinental blocks. Eventually, two overlapping rift segments surround a rotating block resulting in an asymmetric distribution of predominantly strike-slip and reverse faulting regimes (Figures 8h and 8l).

Further analysis shows that there are significant differences in the crustal thinning of the continental lithosphere between the different models (Figure 9). At 25.8 Myr, the continental margins show a similar thinning factor between the different models (Figures 9a, 9c, and 9e). Subsequently, the crustal thinning factor increases with the strength of the microcontinental blocks (Figures 9b, 9d, and 9f). In other words, the continental margin becomes wider and thinner. The main reason for this is that the microcontinental blocks inhibit rift propagation, allowing the continental margin to extend further. This means that margin geometry

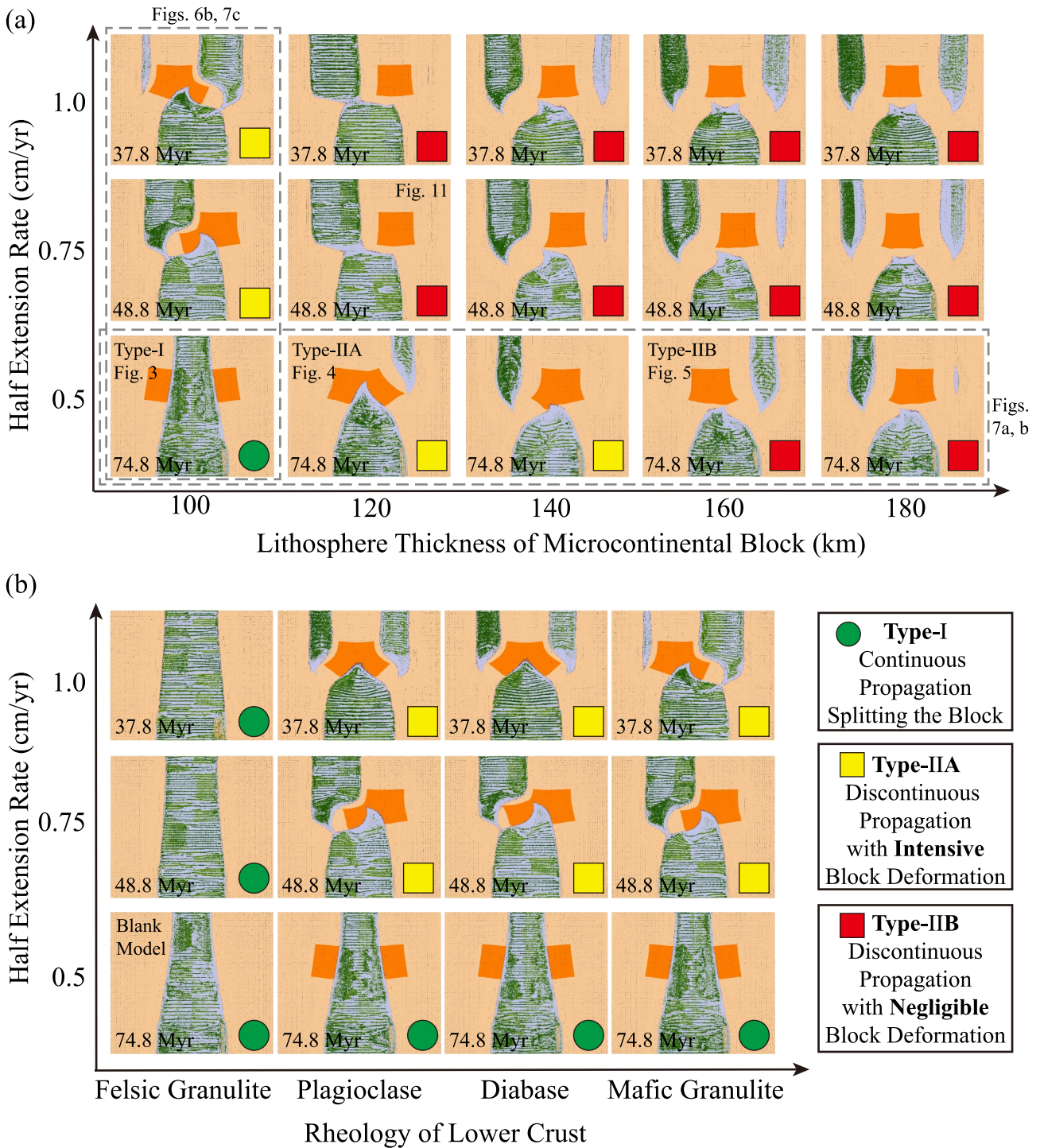
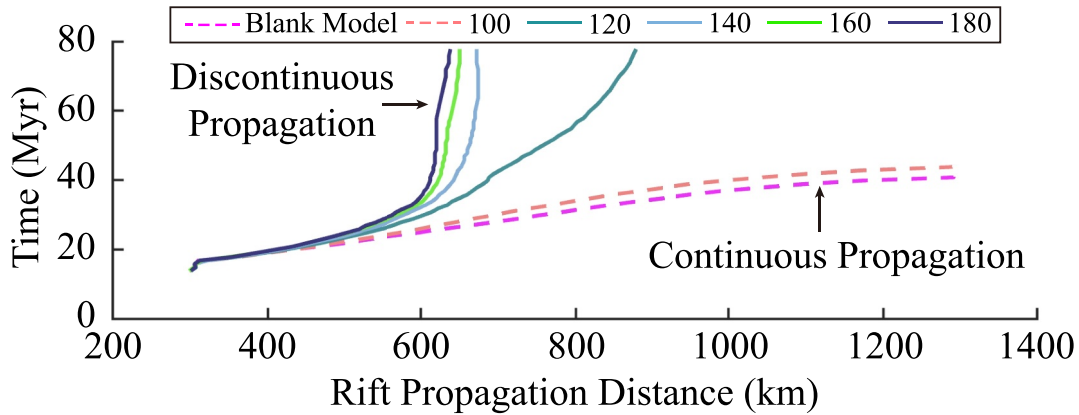
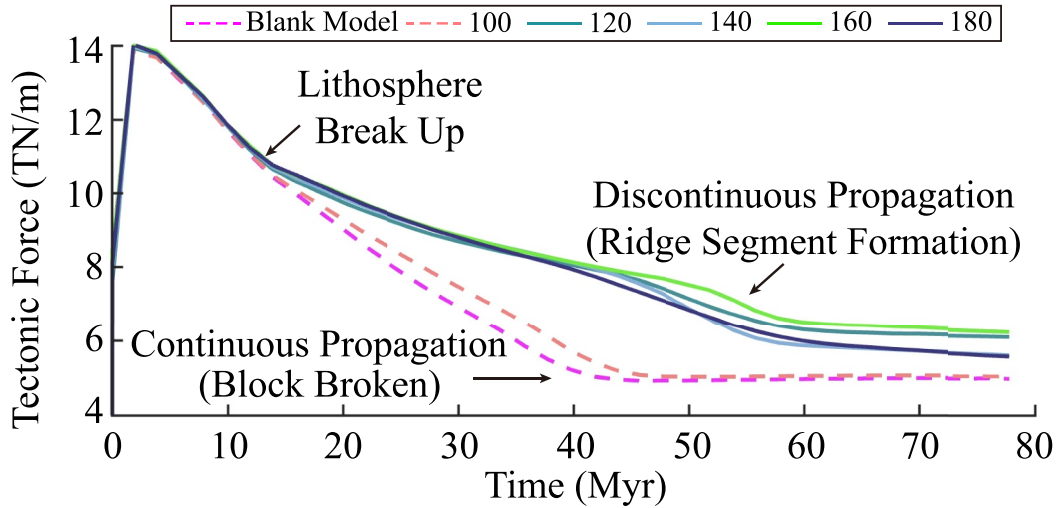


**Figure 6.** Regime diagrams showing three types of rift propagation as a function of lithospheric thickness, rheology of lower crust and extension rate. (a) Regime diagram of microcontinental block lithospheric thickness versus extension rate. (b) Regime diagram of lower crustal rheology versus extension rate. The green, yellow, and red squares represent the different model types. Model results indicate that lithospheric thickness has large influence on rift propagation, while crustal rheology and extension rate have less influence.

(a) *Rift Propagation Distance with Varied Lithospheric Thickness*



(b) *Tectonic Forces with Varied Lithospheric Thickness*



(c) *Tectonic Forces with Varied Half Extension Rate*

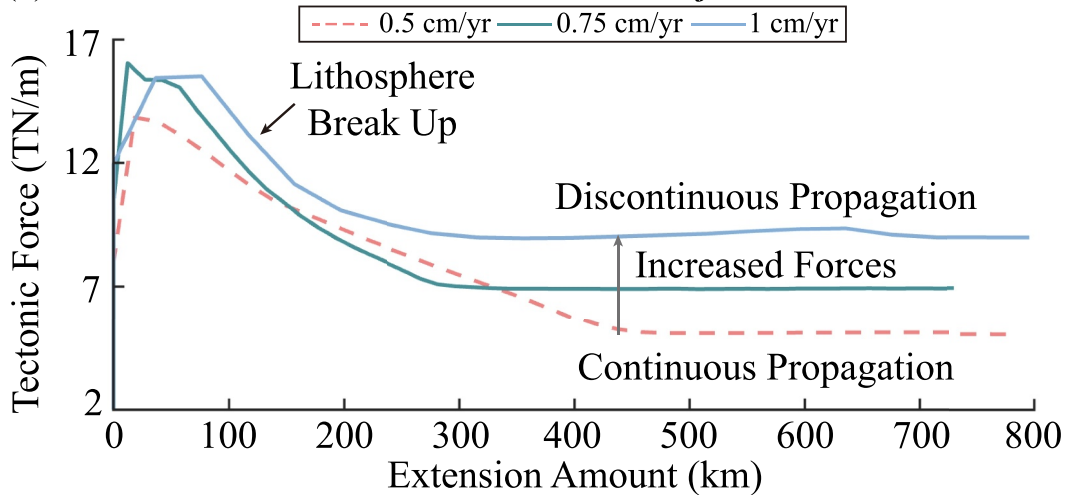


Figure 7.

can be used as a diagnostic feature to assess the relative strength of microcontinental blocks. The resistance of the microcontinental blocks is similar to the far-field compression prescribed in the direction of rift propagation (Le Pourhiet et al., 2018). However, Le Pourhiet et al. (2018) show that the weaker lower crust under far-field compression makes the continental margin wider and thinner. This contrasts with our model results, which show that the strong lower crust and thicker lithosphere of the continental block favor highly localized extension of the continental lithosphere (Figure 9).

## 4. Discussion

### 4.1. Implications for the South China Sea

Two-stage rift propagation, which splits or bypasses microcontinental blocks, has been identified in the South China Sea (Figure 10a). Our model results indicate that the difference in block strength leads to the different types of rift propagation. In the following we interpret this finding in relation to the strength of the microcontinental blocks occurring in the South China Sea margins (Figure 10). Geological data suggests the Xisha Block is stronger than the surrounding blocks: (a) the Xisha Block has Precambrian basement, while the other blocks have younger basement (X. Sun et al., 2014); (b) the crustal thickness of the Xisha Block is about 24–26 km, which is thicker than the other blocks with about 14–20 km (Bai et al., 2015); (c) the crust of the Xisha Block and its surroundings is more mafic than the other blocks (Huang et al., 2011; Li et al., 2021). Taken together, all of these findings align with our model results indicating that the stronger Xisha Block stalled rift propagation in the now-abandoned northwest basin. Subsequently, the relatively weaker blocks (i.e., Zhongsha Block, Reed Bank, Zhongjian Block, Zhenghe Block) were split by the rift propagation (Figure 10a).

In map view, the width of the continental margin increases from 400 to 1,200 km from east to west (Figure 10a). The linear trend of the overall extension is disrupted by the strong Xisha block (Figure 10c). Based on our model results (Figure 10b), we speculate that the wide margin and the alternately varied width are related to the difference in the strength of the microcontinental blocks. Microcontinental blocks (i.e., Xisha Block, Zhongsha Block, Reed Bank, Zhongjian Block, Zhenghe Block) will stop rift propagation and promote continental rifting in front of them but will be less thinned themselves (Figure 10c). In addition, there are many troughs around the microcontinental blocks (i.e., Xisha Trough, Zhongsha Trough), which is consistent with our modeling results (Figures 10b and 10d).

### 4.2. Implications for the East African Rift System

The East African Rift constitutes the largest Cenozoic continental rift system worldwide. The Eastern Branch stretches from Afar to the Tanzania divergence, while the Western Branch extends from North Uganda to Mozambique (Figure 11a). Seen on the scale of the entire rift, one can generalize that rifting in the north is older and more mature than in the south of the rift system (Figure 11a, Macgregor, 2015). This is in agreement with relatively stable plate kinematics since 12 Ma (Iaffaldano et al., 2014) that can be described by counter-clockwise rotation of Somalia and Rovuma relative to Nubia (Stamps et al., 2021). The comparison of present-day faults and the modeling results (Figures 11b–11d), shows that the microcontinental block models successfully capture first-order rift propagation features and block rotation kinematics. Microcontinental blocks inhibit rift propagation, allowing new rifts to develop around the block and subsequently propagate to the sides (Figure 11c). Similar features can be seen in the East African Rift System, where some rifts have propagated both northward and southward (e.g., in South Ethiopia and Lake Tanganyika, Macgregor, 2015). In addition, the interaction between the ridge segments results in an anti-clockwise rotation (Glerum et al., 2020; Stamps et al., 2021) of the rigid

**Figure 7.** Quantifying rift propagation kinematics and tectonic forces for all model scenarios. (a) Rift propagation distance (defined as the position of the propagation tip along the z axis) for models with different lithospheric thickness. A constant half extension rate of 0.5 cm/yr is used in these models. (b) Tectonic forces with varied lithospheric thickness. Again, a constant half extension rate of 0.5 cm/yr is used in these models. (c) Tectonic forces with varied half extension rate. Here we employ a constant lithospheric thickness of 100 km. Discontinuous and continuous rift propagation models are represented by solid and dashed lines, respectively. Quantitative analyses indicate that thick lithosphere reduces the propagation distance and requires a higher tectonic force during model evolution. Similarly, faster extension requires higher tectonic forces, while lower crustal rheology exerts less impact on these quantities.

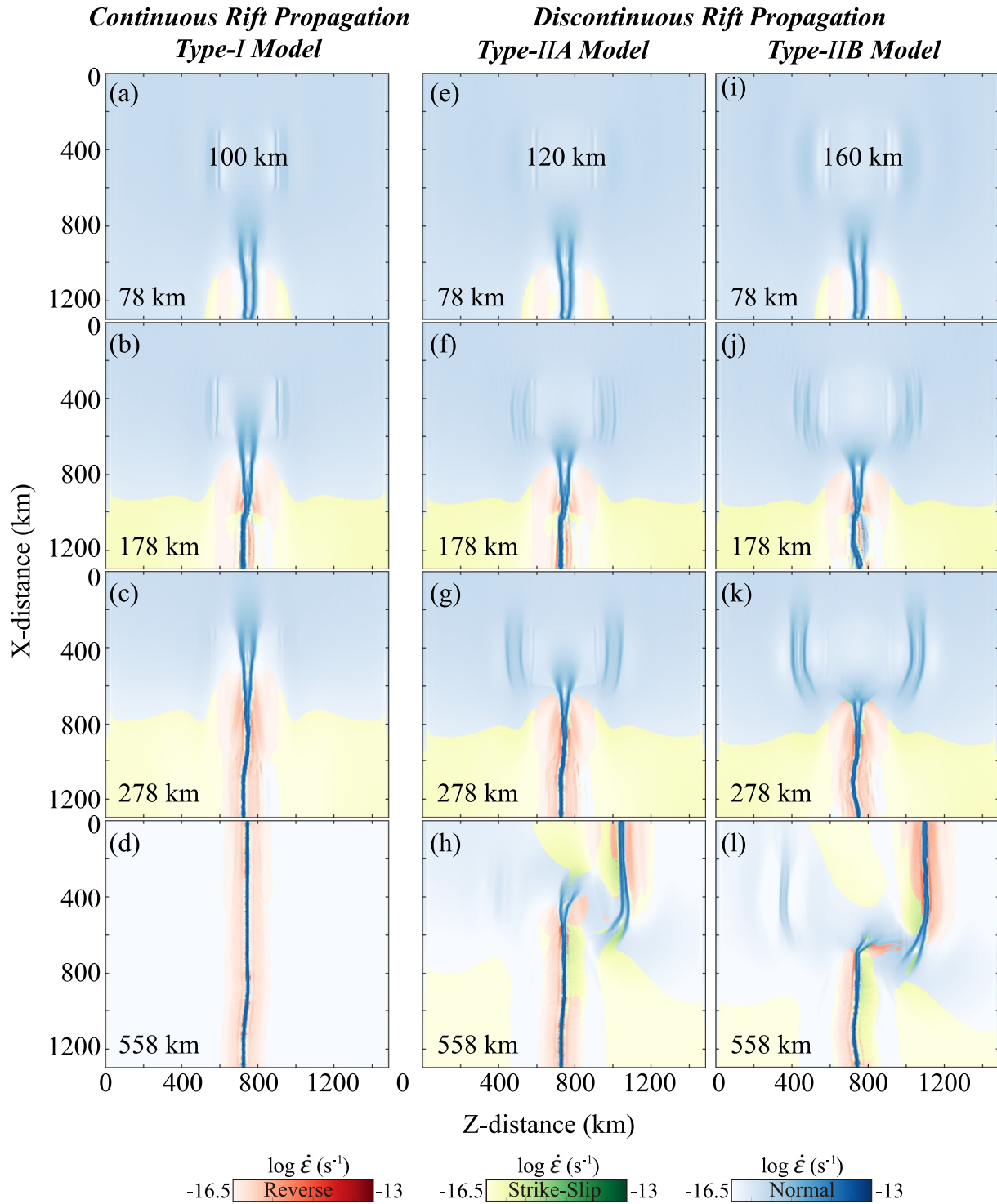


**Figure 8.** Fault patterns of reference models derived by strain rate (with the same amount of extension). (a–d) Continuous rift propagation splitting the microcontinental block. (e–f) Discontinuous rift propagation with intensive block deformation. (g–l) Discontinuous rift propagation with negligible block deformation. Reverse, strike-slip, and normal fault regimes are mapped in red, green, and blue, respectively. The superimposed colors represent the Regime Stress Ratio (e.g., Brune, 2014), whose color saturation is weighted by strain rate (Mondy et al., 2018). Comparison of fault patterns documents significant differences between the fundamental model types.

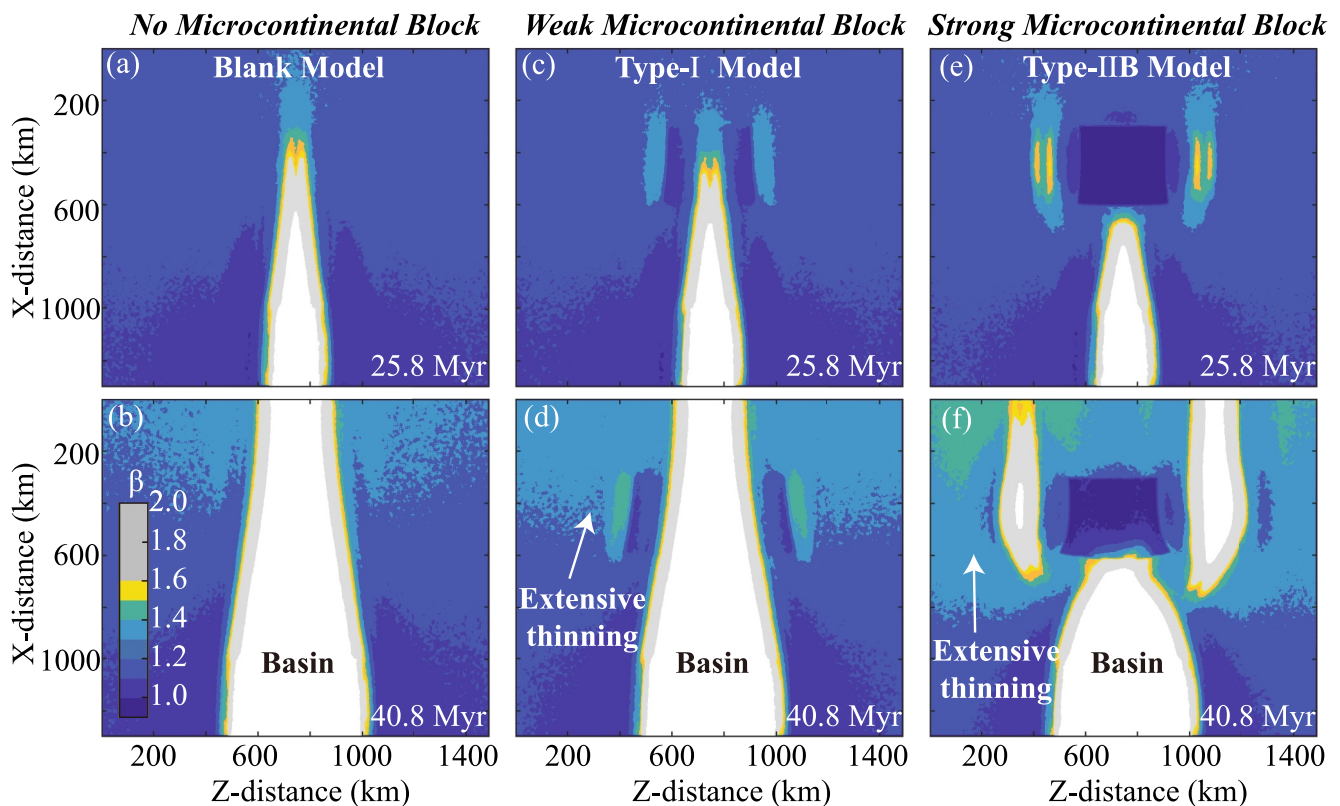


**Figure 9.** Crustal thinning factor ( $\beta$ ) comparison with varied strength microcontinental blocks. (a–b) No microcontinental block model (blank model). (c–d) Weak microcontinental block model (Type-I model). (e–f) Strong microcontinental block model (Type-IIB model). Comparison of the crustal thinning factor indicates that strong microcontinental blocks will inhibit rift propagation and promote the continental margin thinning.

Tanzania Craton (Figure 11d). A limitation of our model is that we do not include precise surface deformation processes, which are important in the East African Rift system with the regional west-east erosion gradient since the Miocene (Sternai et al., 2021; Stüwe et al., 2022).

### 4.3. Implications for the Woodlark Basin

Rift propagation of the Woodlark Basin divided the Papuan Peninsula into the Woodlark and Pocklington Rises (Figure 12a). Overall, the propagation pattern of the Woodlark Basin is similar to that of our Type-I model, but the rift and ridge branches are segmented by several transform and non-transform offsets that are characteristic of the Type-II model. Figures 11b–11d shows a schematic reconstruction (Taylor et al., 2009) of plate boundary evolution in the basin. Spreading segment 2 nucleated at 1.9–2.0 Ma and segment 3 ceased propagating westward by 1.8 Ma. The spreading segments were separated by rifted continental crust prior to the formation of the Moresby Transform at ~1.5 Ma. This is consistent with our model results, which indeed reproduce the characteristics of two spreading centers as well as the presence of the transform fault observed in the Woodlark Basin (Figures 12e–12g). When rift propagation gets stalled by the microcontinental block, a new rift segment nucleates on the other side. Thereafter, a transform fault will form and accommodate the extension of two ridge segments. It should be mentioned that the Papuan Peninsula is not a typical microcontinental block. However, the lithospheric thickness of surrounding rifted margins increases abruptly westward of the Moresby Transform (Martínez et al., 1999), just like in our microcontinental block model.

## 5. Conclusions

We investigate the dynamic evolution of rift propagation as it encounters a microcontinental block by using 3D thermo-mechanical numerical models. Based on the model results, we draw the following conclusions:

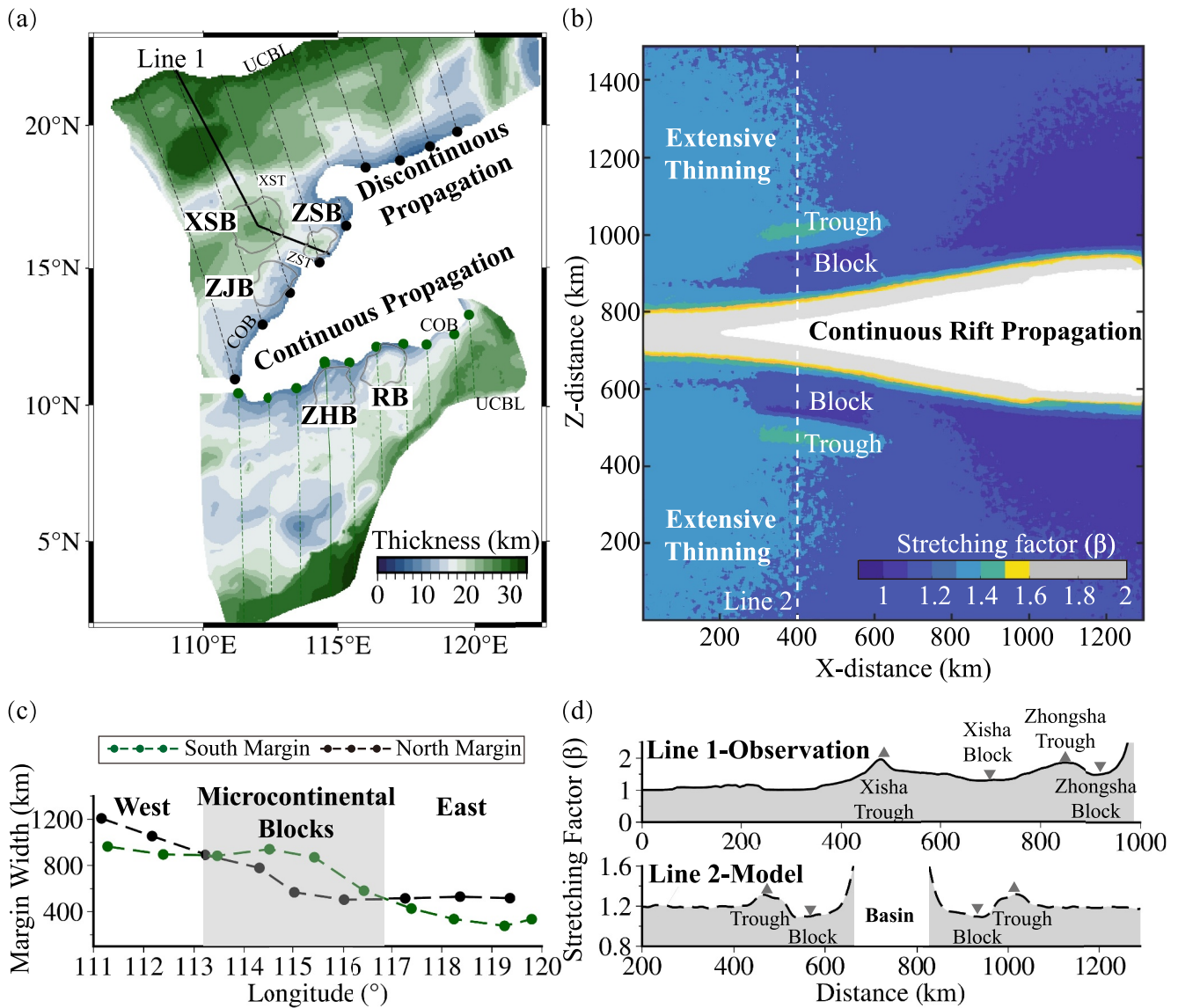


**Figure 10.** Comparison of model results to microcontinental blocks of the South China Sea margin. (a) Crustal thickness of the South China Sea margin (data from Bai et al., 2015). (b) Model results of Type-I model shows increased thinning trend in front of the rift propagation tip. (c) Southern and northern continental margin width of the South China Sea. We used the motion path, continental-oceanic boundary (COB), and the unstretched continental basement limit (UCBL) of the South China Sea margin from Bai et al. (2015) to compute the width of conjugated margins along longitude. (d) Stretching factor extracted from lines 1 and 2, which is positioned across the Xisha Block, Zhongsha Block (Bai et al., 2015) and the microcontinental blocks in our model results. XSB, Xisha Block; ZB, Zhongsha Block; ZJB, Zhongjian Block; ZHB, Zhenghe Block; RB, Reed Bank; XST, Xisha trough; ZT, Zhongsha trough. The black and green circles are the start of the motion path at the continental-ocean boundary. Gray upper and lower triangles indicate a high or low degree of thinning, respectively. These data indicate that the strength of microcontinental blocks controls the pattern of rift propagation in the South China Sea. Microcontinental blocks promote the extension of continental margins, and it is this difference in strength that leads to the formation of troughs.

1. Rift propagation can be affected by pre-existing microcontinental blocks. We propose two types of interaction. The first type is characterized by continuous rift propagation splitting the microcontinental block, while the second type is characterized by discontinuous rift propagation bypassing the microcontinental block and the formation of overlapping ridge segments.
2. The lithospheric thickness of the microcontinental blocks and their associated strength exert first order control on rift propagation patterns. If the lithosphere is thicker, rift propagation tends to be discontinuous. Lower crustal rheology and extension rate may influence rift propagation but play a minor role.



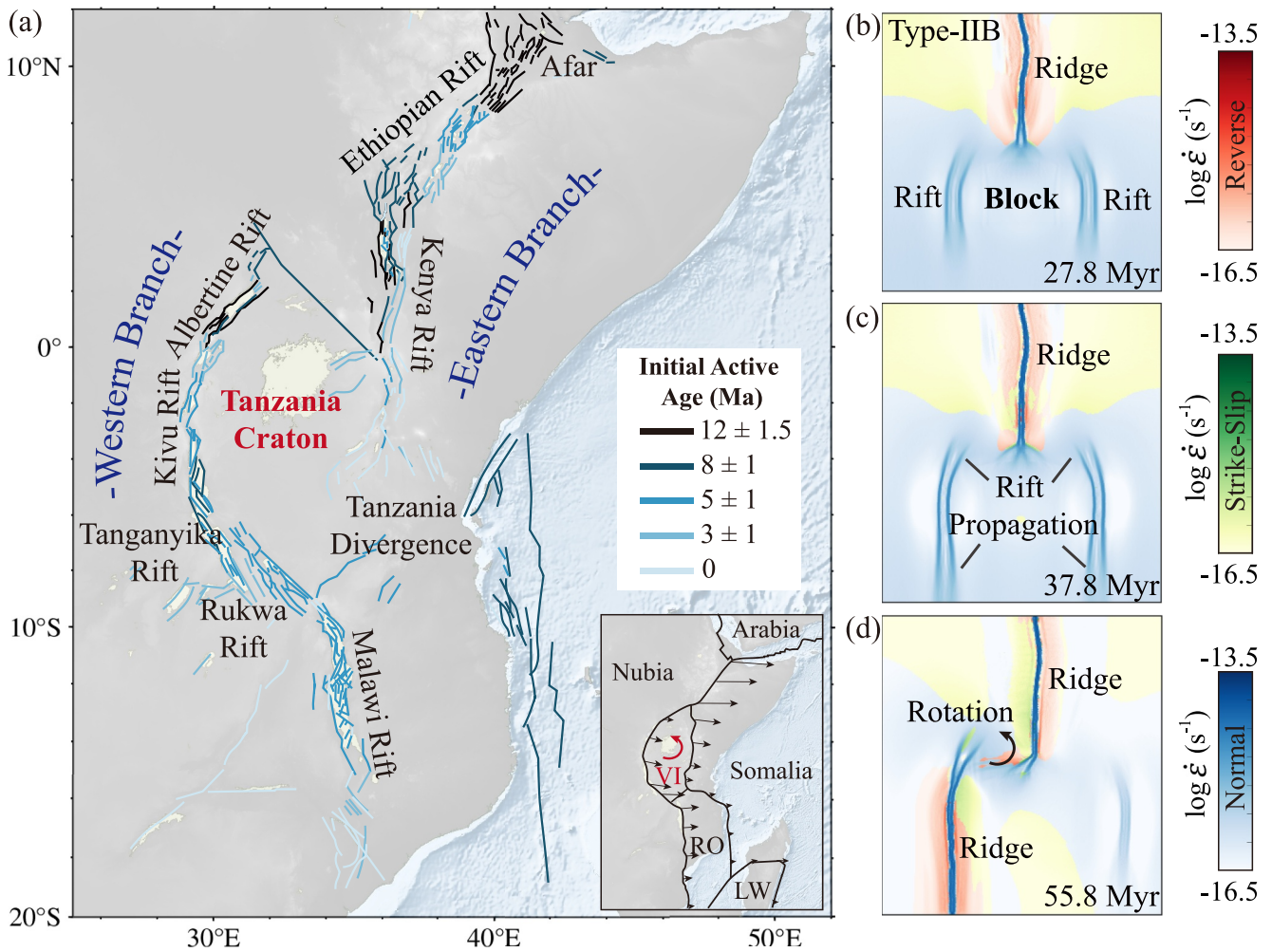


**Figure 11.** Application to the East Africa Rift System. (a) History of the initiation of the East African Rift System (modified from Macgregor, 2015). Different color indicates the initial active age of faults. (b–d) Evolution of modeled fault patterns derived from strain rate. The superimposed colors represent the regime stress ratio, whose color saturation is weighted by strain rate. During the process of rift propagation, strong microcontinental blocks like the Victoria block that is underlain by the Archean Tanzania Craton deflect rift localization to regions adjacent of the block. Conversely, the microcontinental block is affected by the geometry of overlapping rift branches that for right-lateral stepovers produce counter-clockwise block rotation. Abbreviations: Victoria (VI), Rovuma (RO), Lwandle (LW).

3. There are significant differences in stress regime patterns and fault evolution between the reference models, most notably in terms of normal and strike-slip faults adjacent to microcontinental blocks. Microcontinental blocks promote the extension of continental margins, and it is this difference in strength that leads to the formation of troughs.
4. The presence of weak microcontinental blocks, such as the Zhongsha block in the South China Sea, leads to continuous rift propagation. The Tanzania craton represents a strong microcontinental block that cannot be split by rift propagation and instead influences surrounding fault patterns. The strong continental margins of the Woodlark Basin act like strong blocks that also inhibit rift propagation.

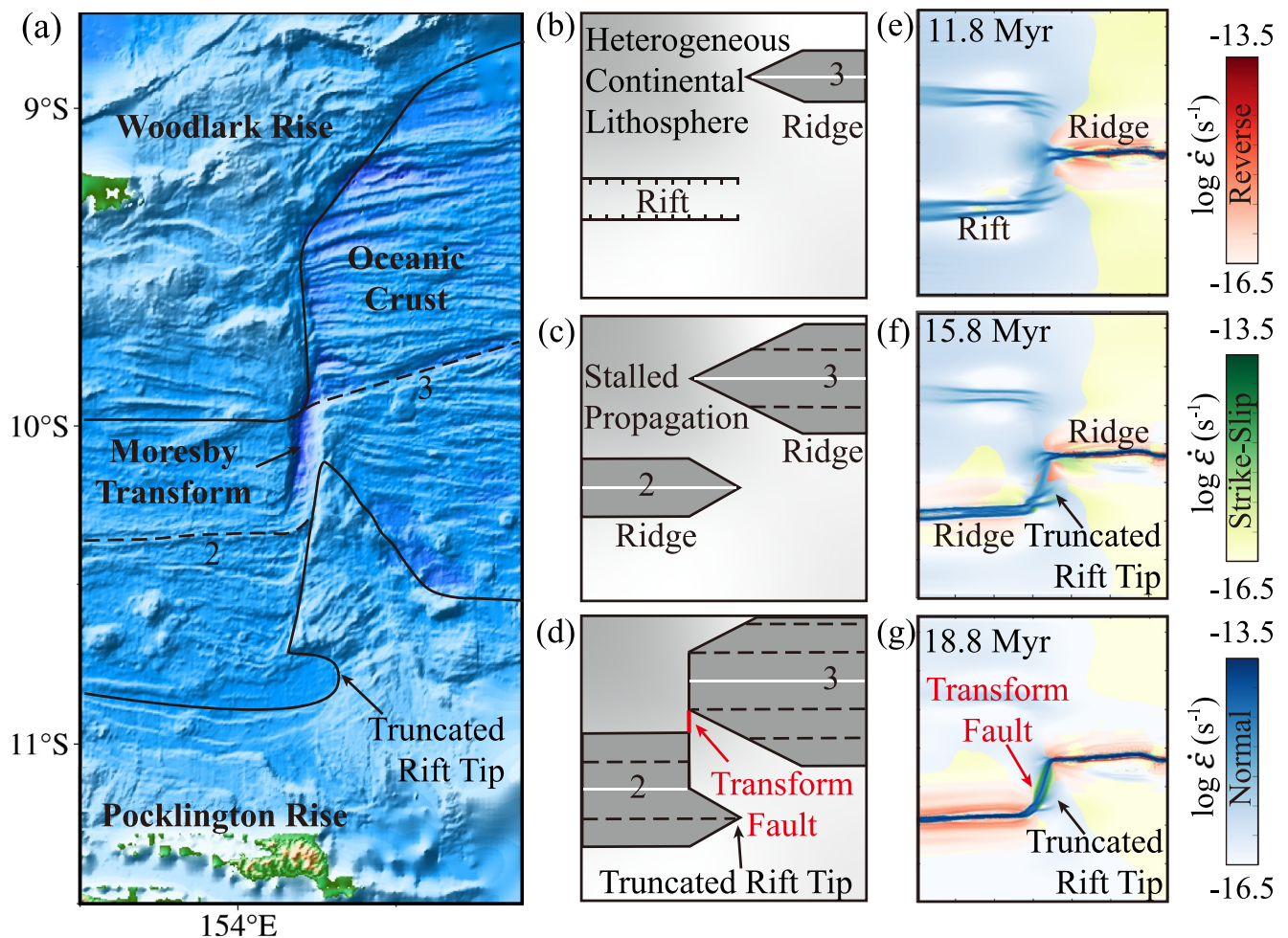


**Figure 12.** Comparison of model and natural data for the rift propagation in the Woodlark basin. (a) Topography of the Moresby Transform fault and its conjugate margins in the Woodlark basin. (b–d) Schematic evolution of the rift propagation in the Woodlark basin (modified from Taylor et al., 2009). Heterogeneous continental lithosphere is indicated by different shades of gray. (e–g) Evolution of fault patterns derived from strain rate. The superimposed colors represent the regime stress ratio, whose color saturation is weighted by strain rate. We conclude that strong continental margins can act like microcontinental blocks also inhibiting rift propagation.

### Conflict of Interest

The authors declare no conflicts of interest relevant to this study.

### Data Availability Statement

All related data of the numerical models are provided in Zenodo (Qing et al., 2023). Free software packages Generic Mapping Tools (GMT) version 6 (Wessel et al., 2013), Matplotlib (Hunter, 2007), Paraview (Ahrens et al., 2005) are used for creating the figures.

### References

- Abera, R., Van Wijk, J., & Axen, G. (2016). Formation of continental fragments: The Tamayo Bank, Gulf of California, Mexico. *Geology*, *44*(8), 595–598. <https://doi.org/10.1130/G38123.1>
- Ahrens, J., Geveci, B., Law, C., Hansen, C., & Johnson, C. (2005). 36-paraview: An end-user tool for large-data visualization. *The Visualization Handbook*, *717*, 50038–50041.
- Audet, P., & Bürgmann, R. (2011). Dominant role of tectonic inheritance in supercontinent cycles. *Nature Geoscience*, *4*(3), 184–187. <https://doi.org/10.1038/ngeo1080>
- Bai, Y., Wu, S., Liu, Z., Müller, R. D., Williams, S. E., Zahirovic, S., & Dong, D. (2015). Full-fit reconstruction of the South China Sea conjugate margins. *Tectonophysics*, *661*, 121–135. <https://doi.org/10.1016/j.tecto.2015.08.028>
- Balázs, A., Gerya, T., May, D., & Tari, G. (2023). Contrasting transform and passive margin subsidence history and heat flow evolution: Insights from 3D thermo-mechanical modelling. *Geological Society, London, Special Publications*, *524*(1), 191–217. <https://doi.org/10.1144/SP524-2021-94>

### Acknowledgments

We thank Taras Gerya for his long-lasting guidance on our geodynamical modeling. Jie Liao acknowledges funding from NSFC projects (42222406, U1901214, 41974104). Sascha Brune has been funded by the European Union (ERC, EMERGE, 101087245). We thank Linfeng Liao, Chengfei Wu for their constructive suggestion which improved this work. We thank Yongliang Bai for the permission to publish the higher resolution crustal thickness data for the South China Sea margin. Numerical simulations were run on the clusters of National Supercomputer Center in Guangzhou (Tianhe-II).

- Bellahsen, N., Faccenna, C., Funicello, F., Daniel, J. M., & Jolivet, L. (2003). Why did Arabia separate from Africa? Insights from 3-D laboratory experiments. *Earth and Planetary Science Letters*, *216*(3), 365–381. [https://doi.org/10.1016/S0012-821X\(03\)00516-8](https://doi.org/10.1016/S0012-821X(03)00516-8)
- Briais, A., Patriat, P., & Tapponnier, P. (1993). Updated interpretation of magnetic anomalies and seafloor spreading stages in the South China Sea: Implications for the Tertiary tectonics of Southeast Asia. *Journal of Geophysical Research*, *98*(B4), 6299–6328. <https://doi.org/10.1029/92JB02280>
- Brune, S. (2014). Evolution of stress and fault patterns in oblique rift systems: 3-D numerical lithospheric-scale experiments from rift to breakup. *Geochemistry, Geophysics, Geosystems*, *15*(8), 3392–3415. <https://doi.org/10.1002/2014GC005446>
- Brune, S., Kolawole, F., Olive, J.-A., Stamps, D. S., Buck, W. R., Buitter, S. J. H., et al. (2023). Geodynamics of continental rift initiation and evolution. *Nature Reviews Earth & Environment*, *4*(4), 235–253. <https://doi.org/10.1038/s43017-023-00391-3>
- Burg, J.-P., & Gerya, T. V. (2005). The role of viscous heating in Barrovian metamorphism of collisional orogens: Thermomechanical models and application to the Lepontine Dome in the Central Alps. *Journal of Metamorphic Geology*, *23*(2), 75–95. <https://doi.org/10.1111/j.1525-1314.2005.00563.x>
- Clauser, C., & Huenges, E. (1995). Rock physics and phase relations. In *A handbook of physical constants* (Vol. 3, pp. 105–126). Courtilot, V. (1982). Propagating rifts and continental breakup. *Tectonics*, *1*(3), 239–250. <https://doi.org/10.1029/TC001i003p00239>
- Cramer, F., Schmeling, H., Golabek, G. J., Duretz, T., Orendt, R., Buitter, S. J. H., et al. (2012). A comparison of numerical surface topography calculations in geodynamic modelling: An evaluation of the ‘sticky air’ method: Modelling topography in geodynamics. *Geophysical Journal International*, *189*(1), 38–54. <https://doi.org/10.1111/j.1365-246X.2012.05388.x>
- Ding, W., & Li, J. (2016). Propagated rifting in the Southwest sub-basin, South China Sea: Insights from analogue modelling. *Journal of Geodynamics*, *100*, 71–86. <https://doi.org/10.1016/j.jog.2016.02.004>
- Dunbar, J. A., & Sawyer, D. S. (1996). Three-dimensional dynamical model of continental rift propagation and margin plateau formation. *Journal of Geophysical Research*, *101*(B12), 27845–27863. <https://doi.org/10.1029/96JB01231>
- Gerya, T. V. (2013). Three-dimensional thermomechanical modeling of oceanic spreading initiation and evolution. *Physics of the Earth and Planetary Interiors*, *214*, 35–52. <https://doi.org/10.1016/j.pepi.2012.10.007>
- Gerya, T. V., & Yuen, D. A. (2003). Characteristics-based marker-in-cell method with conservative finite-differences schemes for modeling geological flows with strongly variable transport properties. *Physics of the Earth and Planetary Interiors*, *140*(4), 293–318. <https://doi.org/10.1016/j.pepi.2003.09.006>
- Glerum, A., Brune, S., Stamps, D. S., & Strecker, M. R. (2020). Victoria continental microplate dynamics controlled by the lithospheric strength distribution of the East African Rift. *Nature Communications*, *11*(1), 2881. <https://doi.org/10.1038/s41467-020-16176-x>
- Gouiza, M., & Naliboff, J. (2021). Rheological inheritance controls the formation of segmented rifted margins in cratonic lithosphere. *Nature Communications*, *12*(1), 4653. <https://doi.org/10.1038/s41467-021-24945-5>
- Heron, P. J., & Pysklywec, R. N. (2016). Inherited structure and coupled crust-mantle lithosphere evolution: Numerical models of Central Australia. *Geophysical Research Letters*, *43*(10), 4962–4970. <https://doi.org/10.1002/2016GL068562>
- Huang, H., He, E., Qiu, X., Guo, X., Fan, J., & Zhang, X. (2020). Insights about the structure and development of Zhongsha Bank in the South China Sea from integrated geophysical modelling. *International Geology Review*, *62*(7–8), 1070–1080. <https://doi.org/10.1080/00206814.2019.1653798>
- Huang, H., Qiu, X., Xu, Y., & Zeng, G. (2011). Crustal structure beneath the Xisha Islands of the South China Sea simulated by the teleseismic receiver function method. *Chinese Journal of Geophysics*, *54*(11), 2788–2798. <https://doi.org/10.3969/j.issn.0001-5733.2011.11.009>
- Hunter, J. D. (2007). Matplotlib: A 2D graphics environment. *Computing in Science & Engineering*, *9*(3), 90–95. <https://doi.org/10.1109/MCSE.2007.55>
- Iaffaldano, G., Hawkins, R., & Sambridge, M. (2014). Bayesian noise-reduction in Arabia/Somalia and Nubia/Arabia finite rotations since ~20 Ma: Implications for Nubia/Somalia relative motion: NUBIA/Somalia kinematics. *Geochemistry, Geophysics, Geosystems*, *15*(4), 845–854. <https://doi.org/10.1002/2013GC005089>
- Jourdon, A., Le Pourhiet, L., Mouthereau, F., & May, D. (2020). Modes of propagation of continental breakup and associated oblique rift structures. *Journal of Geophysical Research: Solid Earth*, *125*(9), e2020JB019906. <https://doi.org/10.1029/2020JB019906>
- King, M. T., & Welford, J. K. (2022a). Advances in deformable plate tectonic models: 1. Reconstructing deformable continental blocks and crustal thicknesses back through time. *Geochemistry, Geophysics, Geosystems*, *23*(6), e2022GC010372. <https://doi.org/10.1029/2022GC010372>
- King, M. T., & Welford, J. K. (2022b). Advances in deformable plate tectonic models: 2. Reconstructing the Southern North Atlantic back through time. *Geochemistry, Geophysics, Geosystems*, *23*(6), e2022GC010373. <https://doi.org/10.1029/2022GC010373>
- Koehn, D., Aanyu, K., Haines, S., & Sachau, T. (2008). Rift nucleation, rift propagation and the creation of basement micro-plates within active rifts. *Tectonophysics*, *458*(1–4), 105–116. <https://doi.org/10.1016/j.tecto.2007.10.003>
- Le Pourhiet, L., Chamot-Rooke, N., Delescluse, M., May, D. A., Watremez, L., & Pubellier, M. (2018). Continental break-up of the South China Sea stalled by far-field compression. *Nature Geoscience*, *11*(8), 605–609. <https://doi.org/10.1038/s41561-018-0178-5>
- Li, Y., Huang, H., Grevemeyer, I., Qiu, X., Zhang, H., & Wang, Q. (2021). Crustal structure beneath the Zhongsha Block and the adjacent abyssal basins, South China Sea: New insights into rifting and initiation of seafloor spreading. *Gondwana Research*, *99*, 53–76. <https://doi.org/10.1016/j.jgr.2021.06.015>
- Macgregor, D. (2015). History of the development of the East African Rift System: A series of interpreted maps through time. *Journal of African Earth Sciences*, *101*, 232–252. <https://doi.org/10.1016/j.jafrearsci.2014.09.016>
- Manighetti, I., Tapponnier, P., Courtilot, V., Gruszow, S., & Gillot, P.-Y. (1997). Propagation of rifting along the Arabia-Somalia plate boundary: The Gulfs of Aden and Tadjoura. *Journal of Geophysical Research*, *102*(B2), 2681–2710. <https://doi.org/10.1029/96JB01185>
- Manighetti, I., Tapponnier, P., Gillot, P. Y., Jacques, E., Courtilot, V., Armijo, R., et al. (1998). Propagation of rifting along the Arabia-Somalia plate boundary: Into Afar. *Journal of Geophysical Research*, *103*(B3), 4947–4974. <https://doi.org/10.1029/97JB02758>
- Martínez, F., Taylor, B., & Goodliffe, A. M. (1999). Contrasting styles of seafloor spreading in the Woodlark Basin: Indications of rift-induced secondary mantle convection. *Journal of Geophysical Research*, *104*(B6), 12909–12926. <https://doi.org/10.1029/1999JB900068>
- Molnar, N. E., Cruden, A. R., & Betts, P. G. (2017). Interactions between propagating rotational rifts and linear rheological heterogeneities: Insights from three-dimensional laboratory experiments. *Tectonics*, *36*(3), 420–443. <https://doi.org/10.1002/2016TC004447>
- Mondy, L. S., Rey, P. F., Duclaux, G., & Moresi, L. (2018). The role of asthenospheric flow during rift propagation and breakup. *Geology*, *46*(2), 103–106. <https://doi.org/10.1130/G39674.1>
- Neuharth, D., Brune, S., Glerum, A., Heine, C., & Welford, J. K. (2021). Formation of continental microplates through rift linkage: Numerical modeling and its application to the Flemish Cap and Sao Paulo Plateau. *Geochemistry, Geophysics, Geosystems*, *22*(4), e2020GC009615. <https://doi.org/10.1029/2020GC009615>
- Nyblade, A. A., & Brazier, R. A. (2002). Precambrian lithospheric controls on the development of the East African rift system. *Geology*, *30*(8), 755. [https://doi.org/10.1130/0091-7613\(2002\)030<0755:PLCOTD>2.0.CO;2](https://doi.org/10.1130/0091-7613(2002)030<0755:PLCOTD>2.0.CO;2)

- Pasyanos, M. E., Masters, T. G., Laske, G., & Ma, Z. (2014). LITHO1.0: An updated crust and lithospheric model of the Earth. *Journal of Geophysical Research: Solid Earth*, *119*(3), 2153–2173. <https://doi.org/10.1002/2013JB010626>
- Pichot, T., Delescluse, M., Chamot-Rooke, N., Pubellier, M., Qiu, Y., Meresse, F., et al. (2014). Deep crustal structure of the conjugate margins of the SW South China Sea from wide-angle refraction seismic data. *Marine and Petroleum Geology*, *58*, 627–643. <https://doi.org/10.1016/j.marpetgeo.2013.10.008>
- Prodehl, C., & Mooney, W. D. (2012). *Exploring the Earth's crust: History and results of controlled-source seismology*. Geological Society of America.
- Qing, J., Liao, J., & Brune, S. (2023). Numerical modeling results for 'Rift propagation interacting with pre-existing microcontinental blocks' [Dataset]. Zenodo. <https://doi.org/10.5281/zenodo.10533933>
- Ranalli, G. (1995). *Rheology of the Earth*. Springer Science & Business Media.
- Schmid, T. C., Brune, S., Glerum, A., & Schreurs, G. (2023). Tectonic interactions during rift linkage: Insights from analog and numerical experiments. *Solid Earth*, *14*(4), 389–407. <https://doi.org/10.5194/se-14-389-2023>
- Seton, M., Whittaker, J. M., Wessel, P., Müller, R. D., DeMets, C., Merkuriev, S., et al. (2014). Community infrastructure and repository for marine magnetic identifications. *Geochemistry, Geophysics, Geosystems*, *15*(4), 1629–1641. <https://doi.org/10.1002/2013GC005176>
- Sibuet, J.-C., Yeh, Y.-C., & Lee, C.-S. (2016). Geodynamics of the South China Sea. *Tectonophysics*, *692*, 98–119. <https://doi.org/10.1016/j.tecto.2016.02.022>
- Srivastava, S. P., Sibuet, J.-C., Cande, S., Roest, W. R., & Reid, I. D. (2000). Magnetic evidence for slow seafloor spreading during the formation of the Newfoundland and Iberian margins. *Earth and Planetary Science Letters*, *182*(1), 61–76. [https://doi.org/10.1016/S0012-821X\(00\)00231-4](https://doi.org/10.1016/S0012-821X(00)00231-4)
- Stamps, D. S., Kreemer, C., Fernandes, R., Rajaonarison, T. A., & Rambolamanana, G. (2021). Redefining East African Rift System kinematics. *Geology*, *49*(2), 150–155. <https://doi.org/10.1130/G47985.1>
- Steinberger, B., Bredow, E., Lebedev, S., Schaeffer, A., & Torsvik, T. H. (2019). Widespread volcanism in the Greenland–North Atlantic region explained by the Iceland plume. *Nature Geoscience*, *12*(1), 61–68. <https://doi.org/10.1038/s41561-018-0251-0>
- Sternai, P., Muller, V. A. P., Jolivet, L., Garzanti, E., Corti, G., Pasquero, C., et al. (2021). Effects of asthenospheric flow and orographic precipitation on continental rifting. *Tectonophysics*, *820*, 229120. <https://doi.org/10.1016/j.tecto.2021.229120>
- Stüwe, K., Robl, J., Turab, S. A., Sternai, P., & Stuart, F. M. (2022). Feedbacks between sea-floor spreading, trade winds and precipitation in the Southern Red Sea. *Nature Communications*, *13*(1), 5405. <https://doi.org/10.1038/s41467-022-32293-1>
- Sun, X., Zhang, X., Zhang, G., Lu, B., Yue, J., & Zhang, B. (2014). Texture and tectonic attribute of Cenozoic basin basement in the northern South China Sea. *Science China Earth Sciences*, *57*(6), 1199–1211. <https://doi.org/10.1007/s11430-014-4835-2>
- Sun, Z., Zhong, Z., Keep, M., Zhou, D., Cai, D., Li, X., et al. (2009). 3D analogue modeling of the South China Sea: A discussion on breakup pattern. *Journal of Asian Earth Sciences*, *34*(4), 544–556. <https://doi.org/10.1016/j.jseaes.2008.09.002>
- Taylor, B., Goodliffe, A., & Martinez, F. (2009). Initiation of transform faults at rifted continental margins. *Comptes Rendus Geoscience*, *341*(5), 428–438. <https://doi.org/10.1016/j.crte.2008.08.010>
- Van Wijk, J. W., & Blackman, D. K. (2005). Dynamics of continental rift propagation: The end-member modes. *Earth and Planetary Science Letters*, *229*(3–4), 247–258. <https://doi.org/10.1016/j.epsl.2004.10.039>
- Vink, G. E. (1982). Continental rifting and the implications for plate tectonic reconstructions. *Journal of Geophysical Research*, *87*(B13), 10677–10688. <https://doi.org/10.1029/JB087iB13p10677>
- Wei, X., Ruan, A., Zhao, M., Qiu, X., Wu, Z., & Niu, X. (2015). Shear wave velocity structure of Reed Bank, southern continental margin of the South China Sea. *Tectonophysics*, *644–645*, 151–160. <https://doi.org/10.1016/j.tecto.2015.01.006>
- Wessel, P., Smith, W. H. F., Scharroo, R., Luis, J., & Wobbe, F. (2013). Generic mapping tools: Improved version released. *Eos, Transactions American Geophysical Union*, *94*(45), 409–410. <https://doi.org/10.1002/2013EO450001>
- Whittaker, J. M., Williams, S. E., Halpin, J. A., Wild, T. J., Stilwell, J. D., Jourdan, F., & Daczko, N. R. (2016). Eastern Indian Ocean micro-continent formation driven by plate motion changes. *Earth and Planetary Science Letters*, *454*, 203–212. <https://doi.org/10.1016/j.epsl.2016.09.019>
- Zahirovic, S., Seton, M., & Müller, R. D. (2014). The Cretaceous and Cenozoic tectonic evolution of Southeast Asia. *Solid Earth*, *5*(1), 227–273. <https://doi.org/10.5194/se-5-227-2014>
- Zwaan, F., Schreurs, G., & Rosenau, M. (2020). Rift propagation in rotational versus orthogonal extension: Insights from 4D analogue models. *Journal of Structural Geology*, *135*, 103946. <https://doi.org/10.1016/j.jsg.2019.103946>

## References From the Supporting Information

- King, M. T., Welford, J. K., & Peace, A. L. (2020). Investigating the role of the Galicia Bank on the formation of the North West Iberian margin using deformable plate tectonic models. *Tectonophysics*, *789*, 228537. <https://doi.org/10.1016/j.tecto.2020.228537>
- Bott, M. H. P. (1959). The mechanics of oblique slip faulting. *Geological Magazine*, *96*(2), 109–117. <https://doi.org/10.1017/S0016756800059987>
- Anderson, E. M. (1905). The dynamics of faulting. *Transactions of the Edinburgh Geological Society*, *8*(3), 387–402. <https://doi.org/10.1144/transed.8.3.387>